ACSNANO

www.acsnano.org

Effective RNA Delivery with Aggregation-Induced Lipid Backfolding

Guan Wang, Mengtong Wu, Juanjuan Ye, Yazhou Xu, Yuxiao Chen, Caoyun Ju, Xiao Xu,* and Can Zhang*

Cite This: *ACS Nano* 2025, 19, 29416−29429

Read Online

ACCESS | Metrics & More | Article Recommendations | Supporting Information

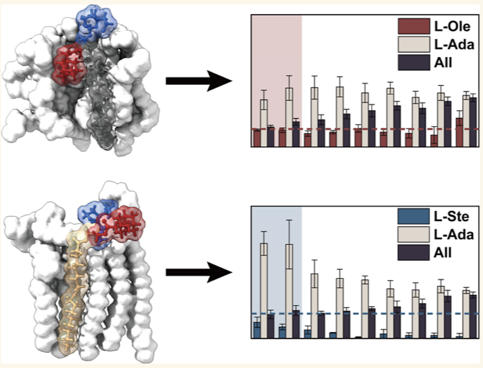

ABSTRACT: **Lipid nanoparticles (LNPs) currently serve as a leading platform for RNA delivery. In this field, endosomal escape of LNPs is a key challenge for efficient RNA therapies. Most current strategies focus on designing ionizable lipids to enhance interactions with endosomal membranes, promoting membrane fusion and RNA release. However, existing methods still rely heavily on time-consuming high-throughput screening, and no effective guidelines for rationally designing ionizable lipid structures have been established. In this study, we propose a lipid structure-based strategy for guiding the LNP formulation. We recommend using lipids with asymmetric hydrocarbon tails, exemplified by L-Ada, which consists of a long oleate chain and a short adamantane group. Through extensive all-atom molecular dynamics simulations, we demonstrate that these asymmetric molecules act as membrane-disrupting agents by inducing lipid back-folding, generating packing defects on the membrane surface that facilitate membrane fusion. To counterbalance the reduced membrane rigidity from significant asymmetry, we propose a formulation combining symmetric and asymmetric-tailed lipids. Our results show that the backfolding effect induced by adamantane aggregation can be effectively controlled by the lipid structure and composition. The optimized formulation, consisting of 20% L-Ada and 80% symmetric lipid L-Ste, achieves a favorable balance between packing defects and membrane rigidity, which is also validated by membrane fusion experiments. A simplified thermodynamic model is further proposed to explain these effects and provides specific guidelines for the design of those lipids. In summary, this study presents LNPs incorporating asymmetrically tailed lipids, demonstrating enhanced membrane fusion capabilities and providing a crucial foundation for the optimization of future LNP formulations.**

KEYWORDS: *asymmetric hydrocarbon tails, lipid backfolding, lipid nanoparticles, endosomal escape, membrane fusion, molecular dynamics simulations*

Gene therapy has gradually become one of the mainstream therapeutic approaches in recent decades, due to its direct targeting of genetic mechanisms.[1] RNA can treat various diseases through mechanisms such as knocking down pathogenic genes and expressing therapeutic proteins, which has led to its widespread application.[2] However, the negative charge of RNA and its instability against ribonucleases result in low delivery efficiency, necessitating the use of delivery vehicles to protect RNA from RNase degradation and renal clearance.[3] Compared to viral vectors, nonviral vectors, with their lower immunogenicity, higher payload capacity, and cost-effectiveness, have emerged as advanced RNA delivery systems.[4−6]

A lipid nanoparticle (LNP), serving as a promising nonviral RNA delivery system, is commonly used for siRNA and mRNA.[7−9] The FDA has also approved patisiran in 2018 and BNT162b2 and mRNA-1273 in 2020, marking the ongoing development and maturity of LNPs as an RNA delivery system.[2] Particularly, following the COVID-19 pandemic and the rising demand for efficient cytosolic delivery of mRNA molecules, there has been a surge in research interest surrounding LNPs as state-of-the-art delivery carriers.[10,11] Despite the continual success LNP delivery achieved, many barriers are still present in realizing the full potential of LNP-RNA systems.[12] Some of these challenges have been overcome through the development and fabrication of LNP, e.g., to increase the load capacity and encapsulation efficiency.[13,14] However, compared with the viral carrier, limitations in transfection efficiency (TE) still remain.[4,15] Reasons for limited

Received: April 29, 2025
Revised: July 22, 2025
Accepted: July 22, 2025
Published: August 5, 2025

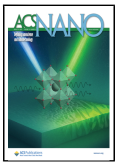

https://doi.org/10.1021/acsnano.5c07140

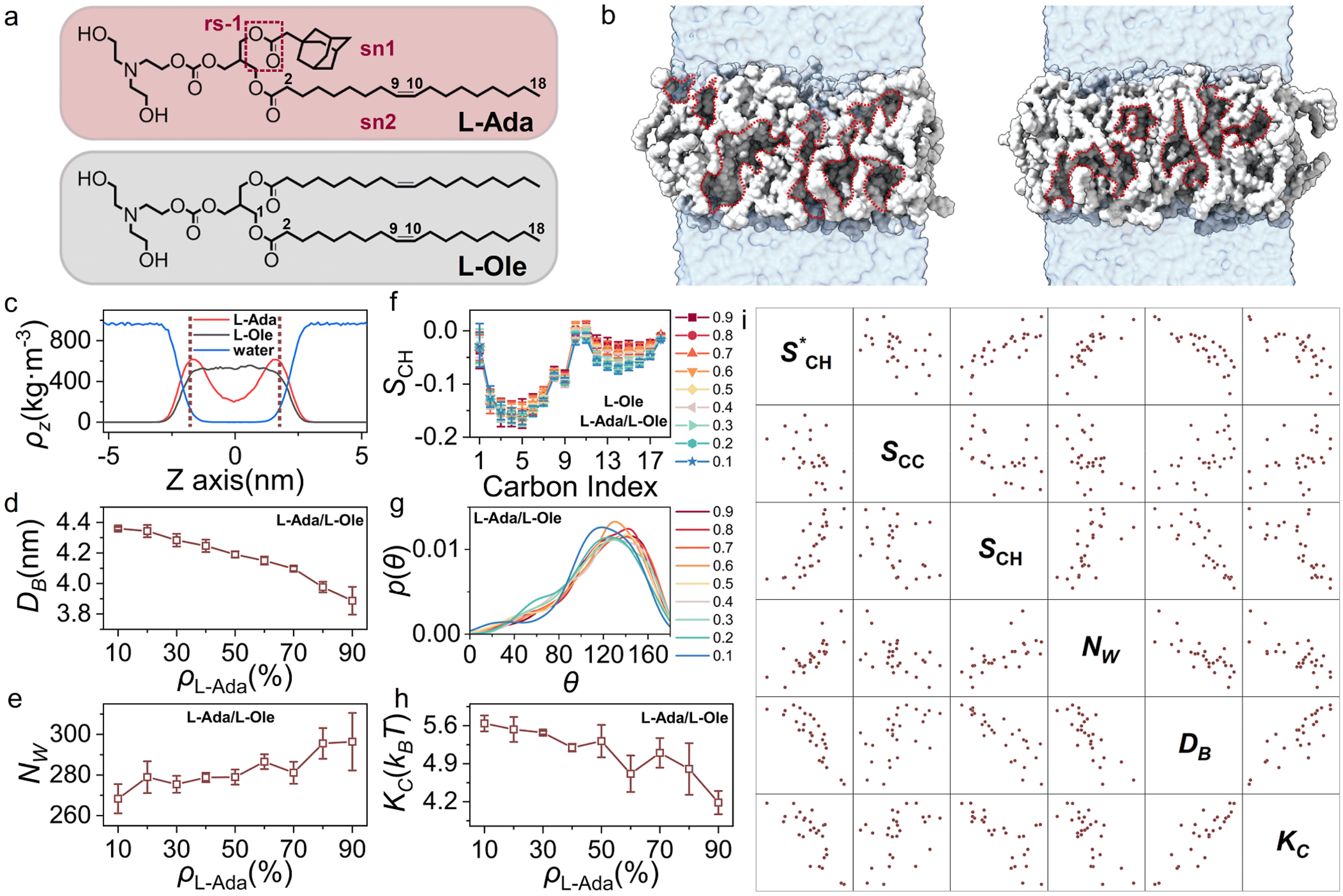

Figure 1. Structural characterization of the L-Ada/L-Ole membranes. (a) Structure of L-Ada (top) and L-Ole (bottom). Snapshots of the simulated L-Ada and L-Ole membrane (b). Lipids are colored white while the water phase is colored semitransparent blue. Packing defects are highlighted with a red dashed line. (c) Density distribution for L-Ada, L-Ole, and water along the membrane normal direction (*z*-axis) in the L-Ada/L-Ole membrane with $\rho_{\text{L-Ada}}$ of 0.5. The membrane Luzzati thickness D_B (d) and the number of penetrated water molecules (N_W) (e) inside the membrane versus the number fraction of the L-Ada lipids ($\rho_{\text{L-Ada}}$). (f) The order parameters S_{CH} of the membrane as a function of the carbon index in lipid tails. (g) The probability distribution function $p(\theta)$ versus the angle θ measuring the angle between the adamantane tails of the lipid and the membrane normal. (h) The membrane bending rigidity K_C monitored by the fraction $\rho_{\text{L-Ada}}$. (i) Orthogonal diagram among measured structural quantities for L-Ada/L-Ole binary membranes.

TE are numerous, while an unsolved bottleneck corresponds to the poor endosomal escape of RNA after the LNP cell entry.[16,17] For efficient delivery, the nucleic acid payloads in the LNP must be released into the cytosol before the maturation of the endosome, in order to avoid the strong enzymatic degradation.[6] At the moment, only 2% or less RNA can eventually enter the cytoplasm.[16] To accelerate the endosomal escape, one approach utilizes the proton buffering capacities of the LNP that results in the influx of chlorine ions, thereby inducing the osmotic rupture of the endosomal membrane.[18] However, pK_a and protonation state prediction suggest the LNP proton sponge effect is very weak,[19] as evidenced by slow membrane expanding of lipid vesicles upon the pH shift from 7.4 to 5.0.[20] As a result, mixing ionogenic lipids with high buffering capacities does not guarantee the high transfection activity of the LNP.[6,21]

The other approach to facilitate the endosomal escape is via the effective membrane fusion,[22,23] that is, to regulate the interaction between the LNP and the luminal side of the endosomal membrane. Concerning anionic lipids presented in the endosomal membrane, cationic or ionizable lipids contained in the LNP are generally optimal.[21] The induced electrostatic attraction may prompt the membranes to approach each other and thus facilitates the membrane fusion, driving the release of the nucleic acid payloads. In that case, experimental evidence has revealed a subsequent subtle structural adjustment, where the membrane switches from the stable lamellar phase to less stable lyotropic liquid crystalline mesophases, such as inverse hexagonal phase and inverse bicontinuous cubic phase, also as a vital step for efficient fusion.[24−28] As a result, the potency of the bilayer for having the phase transition is considered as a marker for efficient endosomal escape.[29−31] Recent studies have shed light on the roles of nonlamellar phases in LNPs, particularly their structural dynamics and implications for RNA delivery efficacy. These insights pave the way for diversified LNP designs that enhance membrane fusion and release, contributing to improved mRNA LNP formulations for broader therapeutic applications. This phase transition correlates with the pK_a value[29,30] and the transition temperature[25,32] of the lipid, which can also be concluded as the lipid structure. Besides, the conical lipid with a small polar head and large hydrophobic tails is also typically favored for the hexagonal phase.[21] For example, the rigid adamantane structure exhibits significant steric hindrance, leading to a characteristic conical structure for adamantane-tailed lipids.[21,33] In our previous research on LNP

https://doi.org/10.1021/acsnano.5c07140
ACS Nano 2025, 19, 29416−29429

formulations designing with high TE, we observed a significant increase (more than 20 times) in TE by adding 15% adamantane-tailed lipid AD8 (L-Ada) during LNP preparation.[34] Although the delicate design of the lipid structure has shown significant improvement of the escape efficiency, at present, there are no quantitative guidelines to devise those lipids. Developing less complex and insightful models is thus necessary to assess the function of those lipids.[6] With this, it will also be possible for us to modify the lipid formulation of the LNPs to achieve enhanced membrane fusion and thus better TE.

Other than the nonlamellar phases, in biological systems, membrane fusion typically depends on specialized fusion proteins, which undergo large conformational changes, including the exposure of hydrophobic fusion peptides, to catalyze the fusion process.[35,36] The above discussion may imply that membrane fusion processes may share a common molecular mechanism, likely involving packing defects within the lipid bilayer.

In this contribution, we present a major step forward in proposing a possible mechanism of membrane fusion and guidelines for designing membrane lipids to facilitate it by analyzing different physical properties of variously composed membrane systems. Based on our previous research, adamantane acetate tail lipid L-Ada and corresponding control lipids were selected as model lipids to construct lipid bilayer membrane systems. By means of extensive all-atom molecular dynamics (MD) simulations, we have summarized the impact of adamantane on membrane physical properties and captured the molecular origin for enhanced TE, which corresponds to the underlying hydrophobic mismatch, giving rise to the backfolding of hydrophobic lipid tails. The hydrophobic membrane defects was reported to be a critical step for membrane fusion.[37,38] By formulating the membrane with lipids of distinct tail structures, for the first time, we propose a practical scheme that may conveniently manipulate the induced hydrophobic defects to achieve the possible LNP formulation with facilitated membrane fusion capacity. Following this, a thermodynamic model summarizing the above effects is finally proposed, which offers a semi-quantitative yet predictive description of the lipid backfolding process, including the guidelines to construct those lipids with designed geometry. Afterward, the model was fully verified by our experimental results.

RESULTS/DISCUSSION

Modeling the L-Ada/L-Ole-Containing Membrane Systems. While the molecular mechanisms underlying membrane fusion remain elusive, certain design principles that facilitate RNA endosomal escape via effective membrane fusion. One approach involves using conical lipids with small polar heads and large hydrophobic tails. In this study, we began by modeling such a lipid, where the large hydrophobic tail is represented by the adamantyl group. The cage structure of the adamantyl group imparts significant steric effects, extreme lipophilicity, and stability—key properties for lipid-mediated RNA delivery. Preliminary results from our previous work have shown that incorporating adamantane into LNPs enhances TE.[34] To gain molecular insights, we modeled the critical adamantane-containing lipid, L-Ada, which is based on a scaffold with an unsaturated oleate chain and the adamantyl group attached at reactive site 1 (Figure 1a). Following experimental setups, we investigated the membranes with or without L-Ada using MD simulations (see the Supporting Information for details). Instead of modeling the entire LNP, which presents computational challenges, we focused on the lipid bilayer, representing a small patch of the LNP's projected enclosure. Compared to membranes without L-Ada, we observed looser lipid packing in the L-Ada-containing membrane, resulting in larger membrane pores and a higher degree of randomness in lipid tail orientation (cf. Figure S1). To further analyze the difference in packing between two membranes, we conducted an analysis of the membrane pore size, defined as the distance between the terminal carbon atom in the lipid hydrophobic tail, by calculating the radial distribution function of water molecules around the terminal carbon atoms of the tail chains (cf. Figure S2). The increase in water distribution indicates a larger pore size due to the presence of L-Ada.

To understand the molecular function of L-Ada, we began with the simplest system by modeling a membrane composed entirely of L-Ada. For comparison, we also studied a membrane containing the conventional phospholipid L-Ole, which is constructed by replacing the adamantane group in L-Ada with a second oleate chain (cf. Figure 1a). This comparison allows us to isolate the specific effects of the adamantane group on the membrane structure and behavior. The simulations demonstrate that both lipids can spontaneously assemble into the membrane structure, although the L-Ada membrane possesses less stability (cf. Figure 1b). Yet, the shorter adamantane tail in L-Ada leads to a core region enriched with less hydrophobic tails compared with the L-Ole membrane, potentially compromising the membrane integrity. The L-Ada membrane possesses more pores, especially in the membrane center (cf. Figure 1b). In this context, formulating LNPs with a high proportion of L-Ada may not be beneficial as membrane integrity is crucial for LNP stability, which in turn affects RNA encapsulation and transport. Regarding the membrane surface, both systems exhibit a layer of densely packed lipid polar heads: the L-Ole bilayer presents a relatively flatter surface, while the L-Ada bilayer is interspersed with numerous adamantane tails (cf. Figures S3 and S4). This configuration for the L-Ada membrane incurs a significant energy penalty by exposing these highly lipophilic groups to an aqueous environment, which we refer to as packing defects afterward. This lipid packing effect is also found for the L-Ole membrane but is particularly pronounced in the L-Ada membrane, where hydrophobic clusters formed by adamantane tails create a stable configuration that may exacerbate the membrane's defects (cf. Figure S5). In the realm of drug delivery, lipid packing defects can be advantageous, particularly as they may facilitate membrane fusion. We therefore anticipate that the exposed adamantane tails promote membrane fusion, potentially contributing to enhanced RNA transfection.

Structural Characterization of L-Ada/L-Ole Membranes. The experimental results demonstrate that incorporating adamantyl lipids with a specific proportion (20%) into LNPs may significantly improve RNA TE through enhancing membrane fusion.[34] To investigate the mechanism of L-Ada proportion affecting TE, we studied more general cases concerning a series of membranes of a binary mixture for lipids L-Ada and L-Ole, with $\rho_{\text{L-Ada}}$ being the number fraction of L-Ada. To preliminarily analyze the construction of membrane systems, we first monitored the positions of the lipids and water using the mass density profile ρ_z, where z

represents the direction of the membrane normal (see Figure 1c). The profile ρ_z clearly indicates the membrane core ($|z| < 1/2\ z_c$) as a region of water depletion, and z_c indicates membrane thickness. Concerning lipids within the membrane core, we observed a constant density for L-Ole, indicating a homogeneous distribution of L-Ole. In contrast, the density for L-Ada exhibits more fluctuations, with an enrichment near the membrane surface, indicating the asymmetric structure of L-Ada. A certain amount of water molecules are also observed in the range of lipids. To investigate the water penetration, we specially plotted the distribution of the water and hydrophobic tails. The density distribution for both water and tail chains in highlighted region are nonzero. This suggests that water can penetrate into the tail region of the upper leaflet of the bilayer (cf. Figure S6).

In terms of the membrane, Luzzati thickness D_B, which indicates the membrane thickness after subtraction of water fraction from z_c (cf. Figure S7), decreases from 4.36 ± 0.01 nm at $\rho_{\text{L-Ada}} = 10\%$ to 3.89 ± 0.09 nm at $\rho_{\text{L-Ada}} = 90\%$ (see Figure 1d). Thereby, we can conclude that the addition of L-Ada significantly gives rise to internal cavities and thus more water fraction in the range of z_c. To evaluate the extent of water penetration, we first measured the number of buried water molecules N_W in the membrane's hydrophobic interior. N_W is maximized in the L-Ada-dominated membrane (cf. Figure 1e), but it is minimized as $\rho_{\text{L-Ada}} = 0.1$ with a majority of L-Oles. Namely, a high accessibility of water and therefore a loose assembly of lipids is captured for the L-Ada-dominated membrane, although the membrane remains a lamellar.

To further analyze the internal construction, the membrane core is characterized by the lipid tail order parameters. Here, S_{CH} represents the average order parameter of all C−H bonds along the acyl chains for lipid L-Ole (cf. Figure 1f) and S^*_{CH} for the acyl chain in L-Ada (cf. Figure S8a). Generally, the S_{CH} profile for L-Ole is consistent with that observed for other common lipids like DOPE, with an increase at carbons 9 and 10 corresponding to the presence of a double bond and a high degree of ordering near the polar headgroup. Notably, the S_{CH} profile remains largely unchanged across membranes with varying $\rho_{\text{L-Ada}}$, indicating that the presence of L-Ada has a minor impact on the packing structure of L-Ole.

Furthermore, to better investigate the packing mode of hydrophobic tails, we measured the bending angle θ to assess the orientation of the adamantane group relative to the membrane normal (see the Methods for details). As shown in Figure 1g, the probability distribution $p(\theta)$ of bending angle θ for the L-Ada adamantane tail is barely sensitive to $\rho_{\text{L-Ada}}$. $p(\theta)$ is enriched at 150°; that is, predominant hydrophobic tails of L-Ada are still well embodied in the membrane indicating suppressed packing defect. With the further addition of L-Oles, the peak of $p(\theta)$ slightly shifts to the left, indicating smaller θ than that of lower L-Ole proportion, and $p(\theta)$ becomes more broadly distributed, signifying a more diverse orientation of the adamantane group at lower $\rho_{\text{L-Ada}}$. The value of $p(\theta)$ slightly increases at 60° with $\rho_{\text{L-Ada}}$ being 0.2 and at 20° with $\rho_{\text{L-Ada}}$ being 0.1. The above observation demonstrates a notable deformation of the L-Ada phase with more L-Oles, which deviates from the stable lamellar phase and forms more significant packing defects. In membranes with more than 80% L-Ole, the orientation for a small fraction of adamantane tails may be restricted to membrane external. Besides, $p(\theta)$ peaked at $\theta \simeq 135°$ in all cases, signifying a persistent overall lamellar structure.

As discussed above, the orientation of lipids is barely well-aligned in L-Ada and L-Ole membranes, indicating a relatively poor packing mode. To investigate its impact on membrane rigidity, we further analyzed the bending rigidity K_C for all systems (cf. Figure 1h). As more L-Ada is involved, the alignment of the hydrophobic layer in the membrane core is disrupted, which leads to lower membrane rigidity. Such observation also indicates that the addition of L-Ada may increase the instability of the membrane structure, which is adverse for the preparation of LNPs.

Notable correlations are found between measured quantities. Here, each data point corresponds to a measure of the simulated membrane, with its x and y coordinates representing certain membrane properties (cf. Figure 1i). Positive correlation is found for S^*_{CH} with S_{CH}. Lower S^*_{CH} or S_{CH} indicates better hydrophobic alignment, which also leads to lower N_W or less water penetration. Besides, as more L-Oles are added, the number of adamantane tails also decreases, which leads to enhanced membrane integrity. Thus, higher membrane thickness D_B and bending rigidity K_c are observed in these membranes. The interplay between these variables highlights the molecular role of L-Ada in a mixed membrane with L-Ole, specifically its capacity to disrupt the lipid packing order and induce packing defects. Notably, the extent of these defects can be modulated by diluting L-Ada within the membrane, offering a valuable strategy for engineering lipid membranes with a controlled degree of packing defects.

Lipid Backfolding Behavior for L-Ada/L-Ole Membranes. By analyzing the distribution of the adamantyl tail, $p(\theta)$, we observed the backfolding state of L-Ada, which means the tail extremity reaches out into the water phase. And thus far, we have only discussed the packing defects mainly caused by the backfolding behavior of adamantyl tails, without assessing the scale and endurance of this phenomenon, which are crucial metrics for evaluating its impact on membrane fusion. Using the carbon C_g at the center of lipid glycerol backbone as the reference atom, we defined a backfolded lipid as one whose tail extremity moves farther from membrane core than C_g (see the Methods for details). In Figure 2a,b, we illustrated the structures of a normal and a backfolded L-Ada in the bilayer, showing a distinct switching of the adamantyl tail toward the polar head and hydrophobic tail, respectively. We first compared the number of backfolding lipids, and a much stronger backfolding tendency was observed in L-Ada than L-Ole (cf. Figure S9). The backfolding probability, $P_{b,i}$, is the average probability measured for each lipid type i from the simulation. For the L-Ada/L-Ole fabricated membrane, we presented the backfolding probabilities $P_{b,\text{L-Ole/L-Ada}}$ for the two lipid components as well as the overall probability $P_{b,\text{all}}$ averaged across all lipids (cf. Figure 2c). Interestingly, both $P_{b,\text{L-Ole}}$ and $P_{b,\text{L-Ada}}$ are above zero, indicating the presence of backfolding in general even for lipids without an adamantane structure. Nevertheless, L-Ada with the adamantane group shows a higher backfolding tendency, with $P_{b,\text{L-Ada}}$ consistently greater than $P_{b,\text{L-Ole}}$ across all systems. This corresponds reasonably to the loosely bound nature of L-Adas, as revealed in our previous structural analysis of the membrane (cf., Figure 1b). In that plot, we measured dependence of the backfolding probabilities for the lipids on the membrane compositions. This observation suggests that the membrane structural variation can influence the stability of the non-backfolded state, thereby modulating the backfolding probability $P_{b,i}$ for both L-Ada and L-Ole lipids. At a high L-Ada

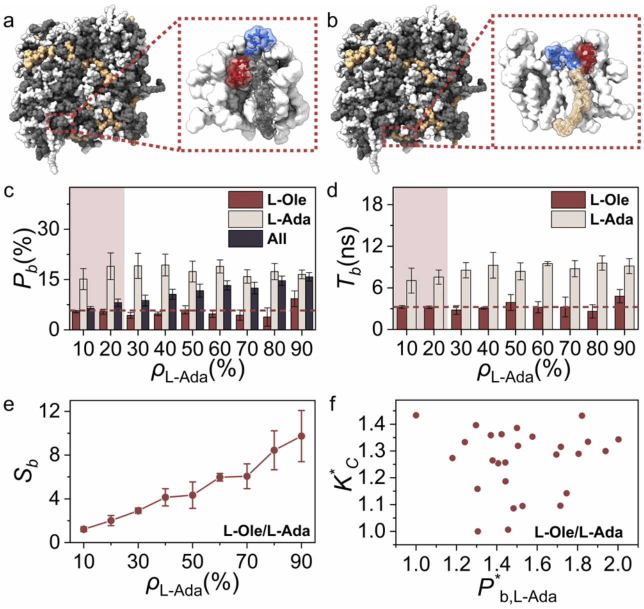

Figure 2. Backfolding properties for the membrane in the mixture of L-Ada and L-Ole lipids. (a,b) The snapshot of the L-Ada/L-Ole membrane with $\rho_{\text{L-Ada}} = 0.5$. The L-Ada lipid without (a) and with (b) the backfolding adamantyl tail are highlighted. The backfolded or normal L-Ada in the membrane is colored in yellow and gray, respectively. For the highlighted L-Ada, its headgroup and the adamantyl tail are colored in blue and red, respectively. Lipid backfolding probability P_b (c) and the backfolding time T_b (d) measured for different lipids. (e) The backfolding cluster size S_b of the L-Ada versus $\rho_{\text{L-Ada}}$. (f) The interplay between the probability $P^*_{\text{b,L-Ada}}$ and membrane bending rigidity K^*_C. Here, $P^*_{\text{b,L-Ada}} = P_{\text{b,L-Ada}}/\min\{P_{\text{b,L-Ada}}\}$ and $K^*_C = K_C/\min\{K_C\}$ are ratios compared to their minimums.

content (e.g., 90%), we observed a drastic increase of $P_{b,i}$ for L-Ole. This may be due to a varying packing structure for a L-Ada dominant membrane, where a higher energetic penalty is applied to the inserted L-Ole due to geometric and packing incompatibilities.

The increase in $P_{b,i}$ also extends the duration, T_b, that a lipid remains in the backfolded state (see Methods for details). In Figure 2d, we show the average $T_{\text{b,L-Ada/L-Ole}}$ for all L-Ada and L-Ole lipids, respectively. Following a trend similar to that of $P_{b,i}$, the backfolding lasts longer for L-Ada than for L-Ole, with $T_{\text{b,L-Ada}} > T_{\text{b,L-Ole}}$ across the entire range of $\rho_{\text{L-Ada}}$. We did not observe any systematic change in $T_{\text{b,L-Ada/L-Ole}}$ with different membrane compositions. Notably, $T_{\text{b,L-Ole}}$ remains similar to the value measured for the pure L-Ole membrane. Therefore, our results suggest that the behavior of L-Ole is hardly influenced by the presence of L-Ada. Beyond the backfolding duration, we also analyzed the formation of backfolded lipid clusters in the membrane (see the Methods and Figure 2e). Specifically, we reported the largest backfolding L-Ada cluster size, S_b, which represents the maximum number of adjacent L-Ada simultaneously backfolding, serving as an indicator of the strength of lipid packing defects. As expected, we observed an increase in S_b from 1.22 to 9.75 as $\rho_{\text{L-Ada}}$ increased from 0.1 to 0.9, indicating more pronounced packing defects with a higher L-Ada content. Although lipid backfolding is highly dynamic, the backfolding clusters can persist within the membrane over the simulation time scale, even though their size fluctuates significantly (cf. Figure S10).

For RNA delivery, an optimal LNP requires a balance between sufficient rigidity for preparation stability and adequate accessibility for membrane fusion. To investigate this, we analyzed the simulated membranes by mapping all systems onto a diagram where the x and y axes represent the lipid-averaged backfolding probability $P_{\text{b,L-Ada}}$, indicating packing defects, and the bending rigidity K_C, representing membrane rigidity (cf. Figure 2f). Each simulated membrane is represented by one data point in the plot. The rescaled parameters $P^*_{\text{b,L-Ada}}$ and K^*_C as compared to their minimums are revealed, increasing from 1 to larger values for most L-Ada/L-Ole membranes. That suggests that adding the L-Adas may impact on the membrane properties; to be exact, it may enhance the lipid backfolding probability and the bending rigidity. While the optimal membrane can be identified at the point with the highest values of both $P_{b,i}$ and K_C, the overall improvement is limited, with only a 100% increase in $P_{\text{b,L-Ada}}$ and a 45% increase in K_C compared to their minimum values. For L-Ole, the changes are even less pronounced. Therefore, varying $\rho_{\text{L-Ada}}$ provides a very limited benefit to the membrane properties in terms of backfolding and rigidity.

Structural Characterization of L-Ada- and L-Ste-Containing Membranes. For the above results, essentially, we demonstrate that the packing defects can be conveniently modulated by changing the lipid composition of the membrane. By changing the proportion of L-Ada, as seen from Figures 1h and 2f, such a modulation is very weak and not effective enough to change the property of the entire membrane. Here, we propose an alternative approach to improve the situation. The general idea is to enhance the membrane integrity while preserving the favorable hydrophobic defects induced by L-Ada. At that point, the L-Ole is replaced with a new lipid type, L-Ste, which has two fully saturated stearic chains as a derivative of L-Ole (cf. Figure 3a bottom). The saturated stearic chains are introduced to provide stronger hydrophobic interactions within the membrane interior, thereby improving membrane integrity, which is well illustrated from the simulated membrane (cf., Figure 3b).

First, the structural properties of the membrane are inspected. Concerning the density profile, we found that L-Ste is enriched within the core area (cf. Figure 3c) as $\rho_{\text{L-Ada}} = 10\%$, and the membrane becomes significantly thinner than that of the L-Ada/L-Ole membrane system with the same $\rho_{\text{L-Ada}}$ (cf. Figure 3d). These results indicate the onset of hydrophobic collapse between the two leaflets due to significantly enhanced hydrophobicity from L-Ste. As more L-Adas are added, leading to fewer long hydrocarbon chains, we first observed an increase in D_B as $\rho_{\text{L-Ada}}$ rises and then a sudden decrease. Inspecting the simulation snapshot, this corresponds to a stepwise separation of the two leaflets, resulting in an increasingly uniform density distribution $\rho_{\text{L-Ste}}$ at the membrane core (cf. Figure S11b). The latter shrinkage is likely due to a reduction in the membrane volume after removal of the long and flexible acyl tails from L-Ste. Interestingly, we observed significant water penetration both at low $\rho_{\text{L-Ada}}$ and high $\rho_{\text{L-Ada}}$ (cf. Figure 3e). Yet, the relevant physical origin is different: at low $\rho_{\text{L-Ada}}$, the buried water arises due to the unique packing style of L-Stes (see Figure S12), while at high $\rho_{\text{L-Ada}}$, N_W grows in response to the expansion of packing defects for an L-Ada-dominant system.

The involvement of L-Ste brings a higher degree of packing order for lipids. With $\rho_{\text{L-Ada}} = 10\%$, we measured the order parameter $S_{\text{CH}} \simeq -0.4$ for L-Ste, suggesting an extremely high

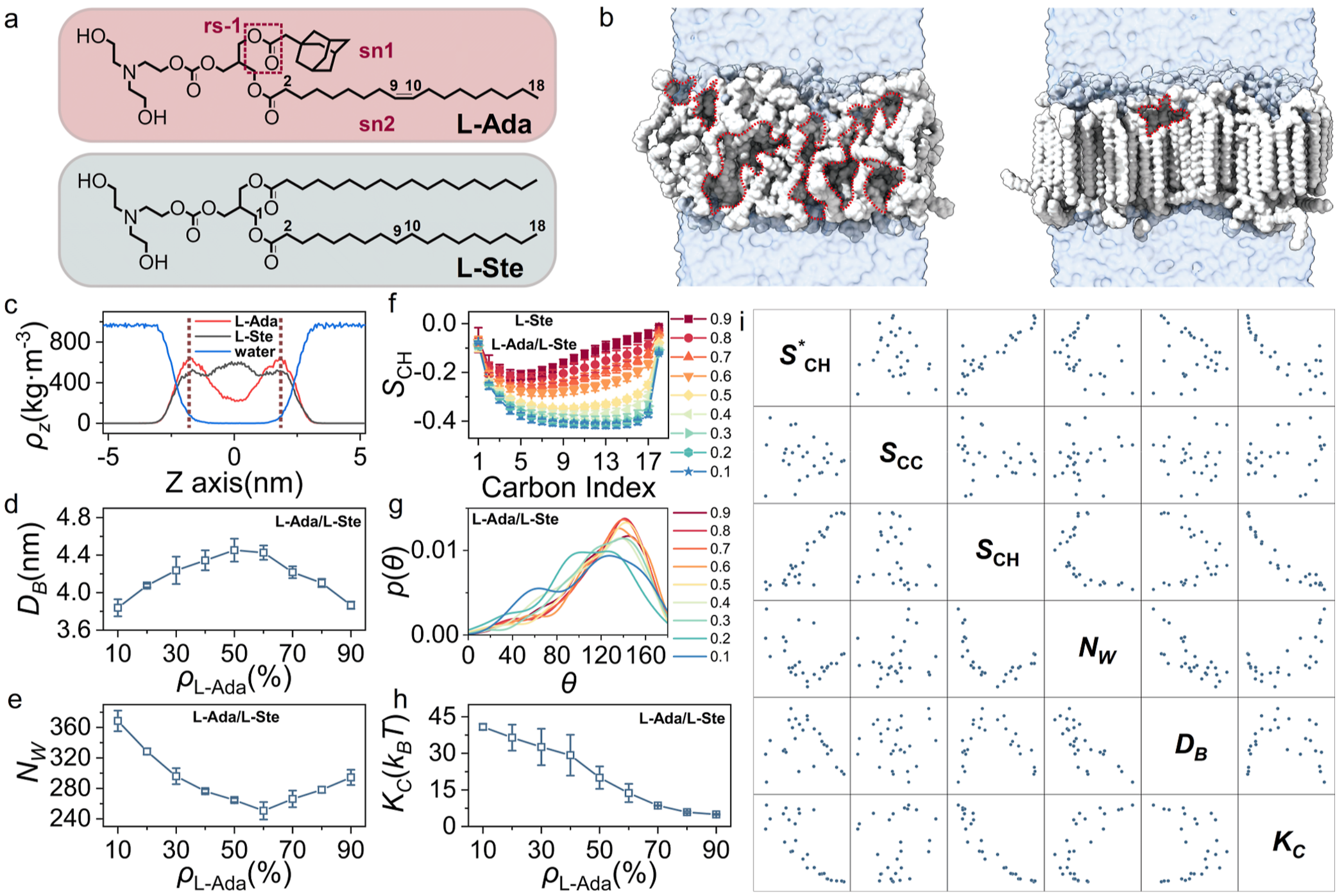

Figure 3. Structural characterization of the L-Ada/L-Ste membrane. (a) Molecular structure of the L-Ada (top) and the L-Ste (bottom) lipid. The snapshot of the simulated L-Ada and L-Ste (b) membrane. The coloring strategy is the same as in Figure 1. (c) Density distribution for L-Ada, L-Ste, and water along the membrane normal direction (*z*-axis) in the L-Ada/L-Ste membrane with $\rho_{L\text{-}Ada}$ = 0.5. The membrane Luzzati thickness D_B (d) and the number of penetrated water molecules (N_W) (e) inside the membrane versus $\rho_{L\text{-}Ada}$. (f) The order parameter S_{CH} of the membrane versus the carbon index in lipid tails. (g) The probability distribution function $p(\theta)$ versus the bending angle θ of the adamantyl tails. (h) The bending rigidity K_C varied with $\rho_{L\text{-}Ada}$. (i) Orthogonal diagram of measured structural quantities for L-Ada/L-Ste membranes.

level of ordering with well-aligned tails (cf. Figure 3f). This ordering becomes disrupted by the L-Ada, as seen by a gradual increase of S_{CH} to −0.2 with more L-Ada, in a way similar to that of the L-Ole involved membrane. Accordingly, concerning the bending angle θ for L-Ada adamantane tail relative to the membrane normal, we already found large angles of $\theta \simeq 130°$ for most L-Ada even with small $\rho_{L\text{-}Ada}$, namely, a high tendency of adamantane tails being excluded to the exterior of the membrane system (cf. Figure 3g). We found a similar behavior for the order parameter for acyl chain in L-Ada, S^*_{CH}, as shown in Figure S8b. Concerning the rigidity of the membrane, generally we found higher K_C for the L-Ste involved system than that with L-Ole (cf. Figure 3h), reasonably in response to the higher degree of packing ordering for L-Ste and consistent with our expectation for introducing L-Ste to the membrane.

The correlation between different properties is illustrated in Figure 3i. Concerning the order parameter S_{CH} of the lipid acyl chain, the increase of S_{CH}, which is primarily driven by the mixture of L-Ste lipids, has varying impacts on the membrane. For instance, the decline of S_{CH} follows a descent of the order parameter for L-Ada sn2 tail, S^*_{CH}, signifying a tight alignment of long acyl chains. Besides, S^*_{CH} and S_{CH} both decrease at higher K_C, which indeed demonstrates a positive correlation between the packing order and the membrane rigidity. Thus, the expectation for a higher membrane rigidity in the presence of L-Ste is justified.

Lipid Backfolding Behavior for L-Ada/L-Ste Membranes. Here, a closer inspection is made for the backfolding behavior of L-Adas in the L-Ste-containing membrane. As expected, the backfolding probability $P_{b,all}$ averaged for all lipids increases with more L-Adas and thus more disruption to the lipid packing. (cf. Figures 4c and S9b). A striking difference we found for the L-Ste-containing membrane as compared to L-Ole's is regarding the dependence of $P_{b,L\text{-}Ada}$ on $\rho_{L\text{-}Ada}$. (cf. Figure 4c). Here, a visible increase of $P_{b,L\text{-}Ada}$ is captured at lower $\rho_{L\text{-}Ada}$, with $P_{b,L\text{-}Ada}$ nearly doubling at $\rho_{L\text{-}Ada}$ = 10% compared to $\rho_{L\text{-}Ada}$ = 90%. These results strongly suggest that the presence of L-Ste facilitates adamantane backfolding. The maximum value of $P_{b,L\text{-}Ada}$ is revealed in the bilayer containing L-Ste rather than L-Ole, which suggests $P_{b,L\text{-}Ada}$ may be enlarged by selecting appropriate lipids cofabricated with L-Ada.

The observed increase in $P_{b,all}$ with rising $\rho_{L\text{-}Ada}$ is primarily attributed to the reduced membrane rigidity introduced by the presence of more L-Ada lipids, which, in turn, facilitates increased randomness in lipid orientation, including backfolding (cf. Figure 3i). In contrast, $P_{b,L\text{-}Ada}$ decreases as $\rho_{L\text{-}Ada}$ increases, suggesting a different mechanism driving L-Ada

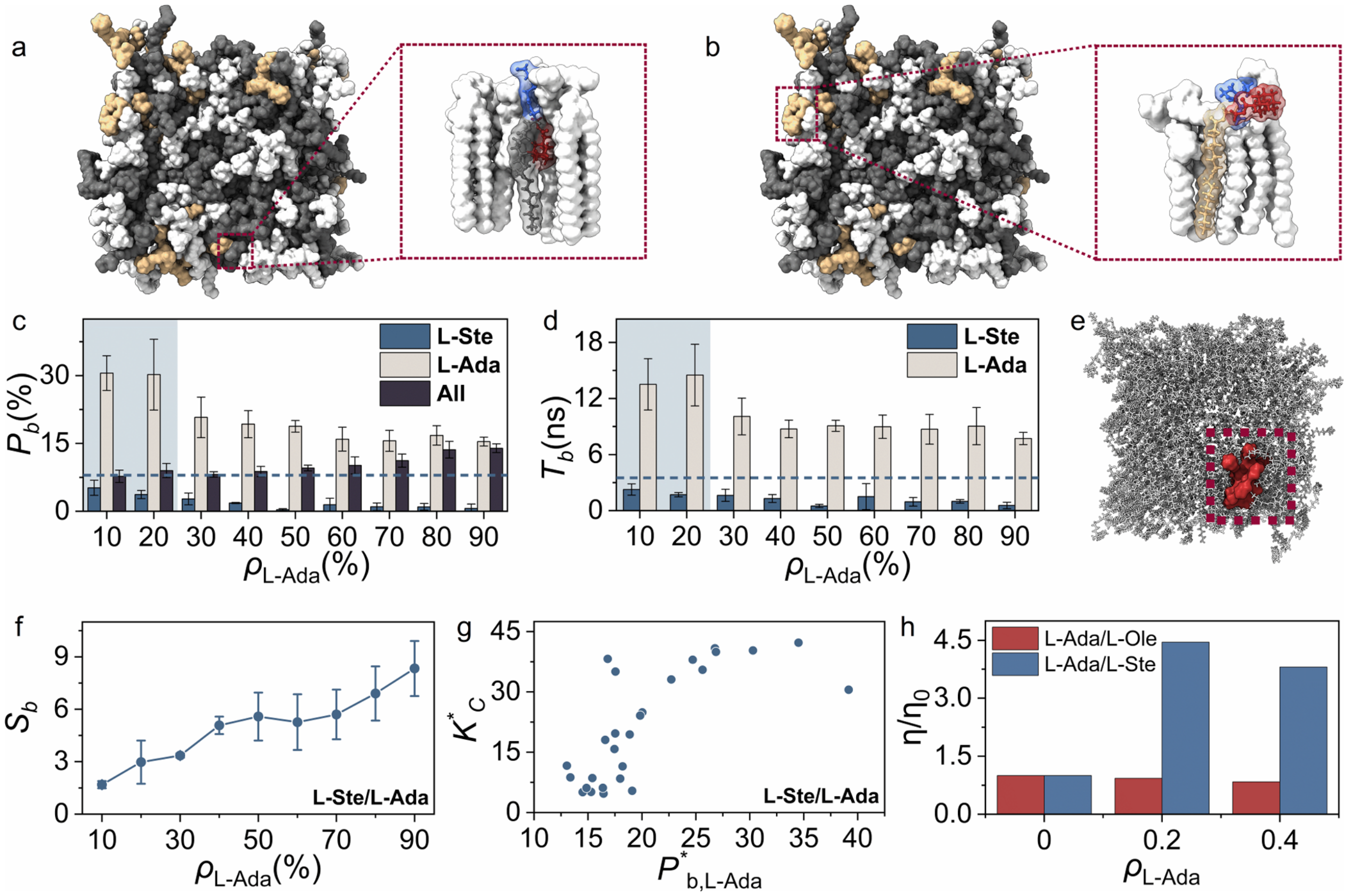

Figure 4. Backfolding properties for the membrane in the mixture of L-Ada and L-Ste lipids. (a,b) The snapshot of the L-Ada/L-Ste membrane with $\rho_{\text{L-Ada}} = 0.5$. The L-Ada lipid without (a) and with (b) the backfolding adamantyl tail are highlighted. The backfolded and normal L-Ada in the membrane are colored in yellow and gray, respectively. For the highlighted L-Ada, its headgroup and the adamantyl tail are colored in blue and red, respectively. Lipid backfolding probability P_b (c) and the backfolding time T_b (d) measured for different lipids. (e) Illustration for the backfolding L-Ada cluster in the L-Ada/L-Ste membrane with $\rho_{\text{L-Ada}} = 0.2$, with backfolding L-Ada in the same cluster colored in red. (f) The backfolding cluster size S_b of the L-Ada versus $\rho_{\text{L-Ada}}$. (g) The interplay between the rescaled probability $P^*_{\text{b,L-Ada}}$ and rescaled membrane bending rigidity K^*_C. Here, $P^*_{\text{b,L-Ada}} = P_{\text{b,L-Ada}}/\min\{P_{\text{b,L-Ada}}\}$ and $K^*_C = K_C/\min\{K_C\}$ are ratios compared to their minimums. (h) The experimentally attained membrane fusion efficiency relative to the efficiency η_0 measured for the pure L-Ole or pure L-Ste membrane, with $\rho_{\text{L-Ada}} = 0$, 0.2, and 0.4.

backfolding, even in a rigid membrane. As shown in Figure 3f, when $\rho_{\text{L-Ada}}$ is between 10 and 20%, the membrane core is predominantly composed of L-Ste, where the lipid acyl tails are well aligned. The backfolding of L-Ada is triggered because the shorter adamantyl tails are generally considered defects in the membrane and are extruded from it. Our results suggest that this aggregation-induced backfolding creates a packing effect much stronger than that observed in L-Ada-dominated membranes, where lipid backfolding emerges from packing randomness. More importantly, the strength of aggregation is critical and is characterized by the hydrophobic collapse of the acyl chains. In our simulations, we observed a higher probability of $P_{\text{b,L-Ada}}$ in membranes composed of L-Ste compared to those with L-Ole, particularly when the fraction of L-Ste in the membrane is high.

With the appropriate lipid formulation, LNPs should exhibit excellent RNA encapsulation and membrane fusion capabilities. We mapped all L-Ada/L-Ste simulation systems onto a diagram, with the x and y axes representing the rescaled lipid-averaged backfolding probability $P^*_{\text{b,L-Ada}}$ and rescaled bending rigidity K^*_C, respectively (cf. Figure 4g). In the L-Ole-involved membrane, we observed a simultaneous increase in both $P^*_{\text{b,L-Ada}}$ and K^*_C, although the extent of the increase is very limited. In contrast, membranes mixed with L-Ste display greater variability across systems with different $\rho_{\text{L-Ada}}$. A key system is identified with increases of approximately 800% in K^*_C and 200% in $P^*_{\text{b,L-Ada}}$ compared to their minimum values, which is significantly higher than that in the L-Ole-containing systems (cf. Figures 2g and S13, S14). These results suggest that membranes cofabricated with L-Ada and L-Ste exhibit properties that are highly favorable for LNP applications, highlighting the potential of engineered lipid formulations for enhanced membrane performance.

Regarding the lipid backfolding time, $T_{\text{b,L-Ole/L-Ada}}$, we observed unique characteristics in the L-Ste-containing systems. Compared to $T_{\text{b,L-Ole}}$ for L-Ole, $T_{\text{b,L-Ste}}$ is significantly reduced across all systems, indicating a strong suppression of backfolding in L-Ste lipids, contributing to membrane stabilization (cf. Figure 4d). In contrast, $T_{\text{b,L-Ada}}$ is much longer than the L-Ole-containing membrane, aligning with the aggregation-induced backfolding process proposed. In this case, L-Ste lipids are tightly locked into the membrane, while L-Ada lipids remain exposed on the membrane surface. As shown in the simulated membranes (cf. Figures S15 and S16),

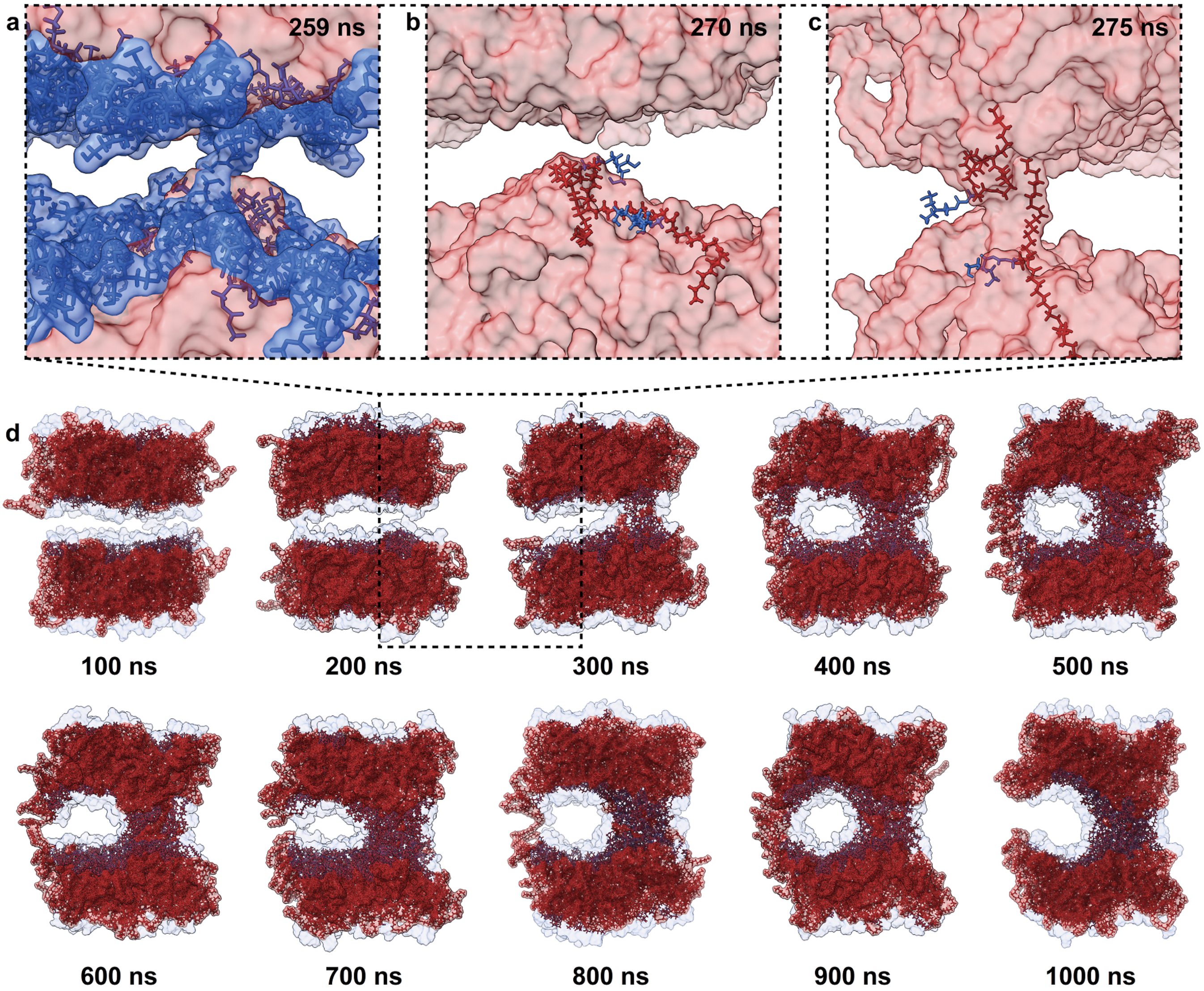

Figure 5. Snapshots of the membrane fusion process. Head groups are represented in blue, and hydrophobic tails are shown in red. The head groups are hidden for better clarity in the snapshots at 270 and 275 ns (b,c).

L-Ada lipids exhibit discrete and slight backfolding in L-Ole-containing membranes, whereas the inclusion of L-Ste results in a more pronounced backfolding effect. Notably, the backfolded L-Ada lipids form patches, with large, connected areas of backfolded lipids emerging in the membrane (cf. Figure S16). Regarding the maximum backfolding patch size, S_b, we observed a monotonic increase in S_b as $\rho_{\text{L-Ada}}$ increases, with the measured S_b exceeding that of the L-Ole-containing membrane, which can also persist throughout the simulation (cf. Figure S10). This indicates a stronger aggregation and backfolding tendency in the L-Ste systems. Due to the structural differences between the lipids, we also investigated the possibility of phase separation for different lipid types. To explore this, we employed more powerful coarse-grained (CG) simulations that extend the accessible time scales and system sizes, enabling a more thorough examination of potential lipid segregation phenomena (see details in the Supporting Information). After simulating for 9 μs, no clear signs of large-scale phase separation were observed, and multiple backfolded clusters remained within the membrane (cf. Figure S17). This is also clearly reflected in the time evolution of the L-Ada cluster size $S_{\text{L-Ada}}$, which remained small throughout the simulation (cf. Figure S18). For other details of the CG simulation, refer to the Supporting Information.

To compare our simulation results with those of experiments, we synthesized LNPs containing the modeled L-Ada, L-Ole, and L-Ste lipids. It is important to note that directly correlating lipid backfolding behavior with experimentally measurable observables remains challenging as cell TE involves numerous stages. Thus, we focused on both the membrane fusion stage and transfection stage, where lipid packing effects are believed to play a critical role. To align with the simulation setup, the LNPs were synthesized with the exact same compositions of L-Ada, L-Ole, and L-Ste as used in the simulations, though this simplified formulation is impractical for omitting other important functional lipids typically involved in LNP design. L-Ada/L-Ole and L-Ada/L-Ste LNPs with $\rho_{\text{L-Ada}}$ as 0, 0.2, and 0.4 are first prepared for further measurements. Detailed methods for LNP preparation are listed in the Supporting Information. The measured fusion and TE are presented in Figures 4h and S19. In L-Ole-containing LNPs, no significant improvement in membrane fusion or TE is observed, as $\rho_{\text{L-Ada}}$ increases from 0 to 0.4. However, in L-Ada/L-Ste membranes, a substantial increase in fusion efficiency, up to 4−5 times (membrane fusion efficiency) and 3−4 times (TE), is achieved with the incorporation of 20% L-Ada. Further increasing L-Ada content to 40% does not result in any additional improvement in membrane fusion. These experimental results align well with the simulation outcomes, particularly the identification of an optimal L-Ada composition around 20%, which maximally enhances lipid backfolding and thus facilitates membrane fusion and transfection.

Characterization of the Membrane Fusion. We conducted detailed AA-MD simulations that monitor the membrane fusion process, from the initial apposition of two bilayers to the formation of the hemifusion stalk. That is applied to membranes composed of a 20% L-Ada and 80% L-Ole mixture. Figure 5 displays representative snapshots from the simulation, taken at 100 ns intervals to illustrate the progression of the fusion process. Notably, the simulation was extended into the microsecond time scale to capture the full course of events leading up to hemifusion.

The simulation trajectory revealed that membrane apposition was achieved in approximately 200 ns, preceding the merger of the proximal monolayers. By around 400 ns, we observed distinct signs of membrane curvature deformation, followed by the onset of a hemifusion stalk, indicating the initiation of membrane fusion. The formation of the stalk is characterized by the localized insertion of hydrophobic lipid segments into both membranes. Notably, our simulation clearly demonstrates that stalk formation is triggered by the establishment of localized hydrophobic contacts between the bilayers.

The simulation also reveals the initial contact between lipid headgroups, which represents the first mechanistic step in membrane fusion. Upon local dehydration and close approach of these polar headgroups, lipid molecules from opposing leaflets begin to bend and merge, then following the connect of the outer leaflets. Our findings are consistent with a broad range of biophysical and experimental studies. Particularly, the simulation revealed backfolding may facilitate the contact between lipid headgroups, which is rationalized by our model in the Supporting Information.

At approximately 275 ns, these initial hydrophobic contacts are formed through the backfolding of L-Ada lipid tails, which become exposed outside the membrane surface (Figure 5c). This "handshake" between the membranes facilitates close apposition and partially overcomes the electrostatic repulsion between charged head groups. For a clearer visualization, the hydrophilic headgroups are hidden in Figure 5b,c, allowing the focus to remain on the full structures of representative lipids and the surrounding hydrophobic tail surfaces. Following this initial contact, expansion of the fusion stalk proceeds and is maintained throughout the subsequent 725 ns of simulation. Our results suggest that lipid backfolding, initialized by those lipids with asymmetric hydrocarbon tails, can initialize the fusion and particularly the formation of the hemifusion-stalk between two membranes. This is in sprit similar to the function of membrane fusion proteins, characterized by its extension state for inserting its fusion peptide to the adjacent membrane.[35,36]

Based on the simulated fusion process, we propose a simplified physical model to understand the beginning of the fusion process when contact is first established through backfolded lipids (see more details in the Supporting Information). To be brief, the two competing forces are modeled in the apposition process of the two membranes: (1) hydrophobic interactions, which promote membrane contact by favoring the exclusion of water at the interface, and (2) electrostatic repulsion, arising from the likely charged nature of the approaching membranes, which tends to resist close contact. We find that the free energy change may decrease with a decreasing membrane separation distance. This suggests that the simulated "handshake" interaction mediated by backfolded lipids can spontaneously promote the close apposition of two membranes. The overall system free energy benefits from minimizing the hydrophobic defect exposed to the solvent as the membranes approach each other, and this energetic gain can outweigh the electrostatic repulsion penalty associated with bringing together two like-charged membranes.

CONCLUSIONS

Endosomal escape through membrane fusion is a critical step for efficient RNA delivery. The presence of hydrophobic defects on the membranes may facilitate the fusion process, where these defects can serve as natural nucleation points for the formation of trans-monolayer contacts. In this work, we demonstrated that an efficient way to trigger pronounced lipid packing defects on the membrane is by incorporating its lipophilic part with adamantane. With extensive atomistic MD simulations, the L-Ada lipids in the membrane exhibit notable backfolding regarding their adamantyl tail, and the exposure of adamantyl groups on the surface gives rise to clustered and sustainable hydrophobic defects on the membrane. In the experiment, we synthesized the corresponding LNP, and the experimental results have confirmed an improved membrane fusion for the LNP mixed with L-Adas.

The nature of packing defects usually relates to a decrease in overall order of the membrane. The structural integrity is disrupted after the addition of L-Ada, as revealed from our calculation of the membrane bending rigidity. The reason relates to the presence of short adamantyl tails, which prevents the alignment of neighboring long and saturated acyl chains that would secure a tight packing of lipids. This effect is not desirable as it may reduce the structural integrity and thus affect the drug encapsulation capacity of the LNP. To solve this problem, we proposed an optimal formulation of the bilayer membrane in the mixture of L-Ada lipids with asymmetric tails as well as symmetric-tailed lipids, leading to a more rigid membrane with tightly packed lipids. A general concern for this strategy is the contaminant suppression of the packing defects given the lipids that are tightly assembled. Fortunately, we did not find this effect in the simulation. As for the membrane containing the L-Ada and the phospholipids L-Ole, the packing defects essentially do not notably change with the composition of L-Ada, apart from the promotion of the membrane rigidity reasonably induced by the mixture of L-Ole. Interestingly, further increasing the lipophilicity of the membrane, as in our case replacing the L-Ole with L-Ste containing two fully saturated acyl chains, we have observed the more pronounced sign of packing defects for L-Ada than that for the pure L-Ada or L-Ada/L-Ole coformulated membrane. To be specific, the simulation has revealed the membrane bearing at maximum 30% of the total L-Ada in the backfolding state, only at the expense of a 20% decrease of the membrane bending rigidity for the pure L-Ste bilayer. This result is appealing, which means the hydrophobic defects can be introduced or enhanced on the LNP surface only with a minor disruption to the LNP structural rigidity.

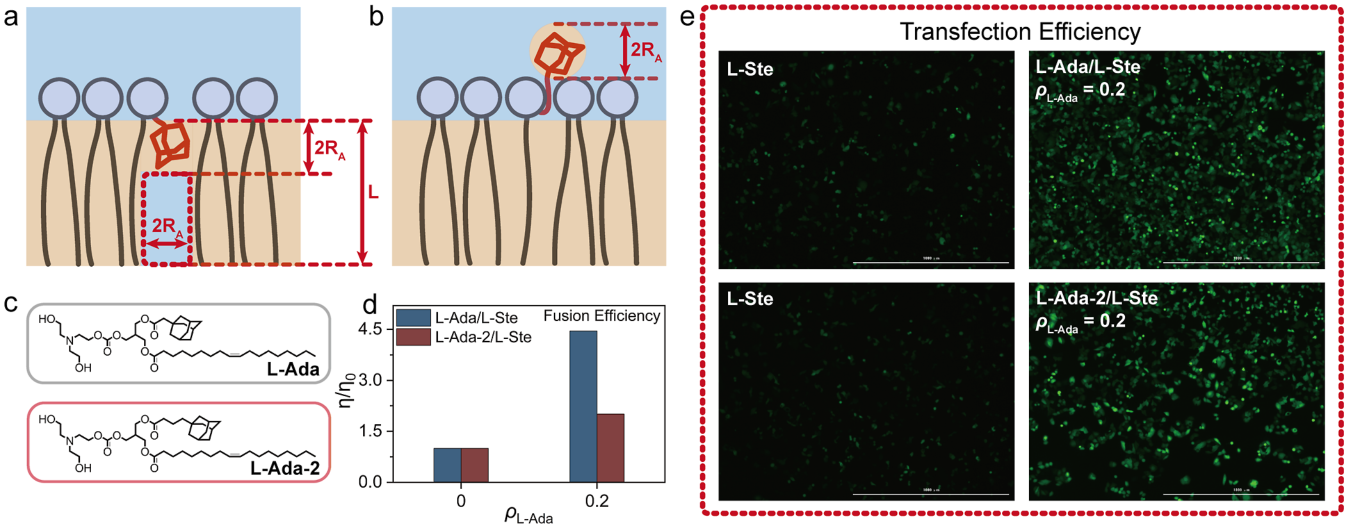

Figure 6. Theoretical model illustration and experimental validation for lipid backfolding. The schematic plot for the lipid in the normal (a) and backfolding (b) state. R_A depicts the radial size of the adamantane considered as a sphere in the modeling. L denotes the length of the long hydrophobic tail of the lipid. (c) Molecular structures of L-Ada and L-Ada-2. (d) The experimentally attained membrane fusion efficiency relative to the efficiency η_0 measured for the membrane for the pure L-Ste membrane, with $\rho_{\text{L-Ada}} = 0$ and 0.2, concerning the L-Ada/L-Ste membranes and L-Ada-2/L-Ste membranes. (e) Fluorescence figures of transfection for L-Ada/L-Ste LNPs with $\rho_{\text{L-Ada}} = 0$ (top left) and 0.2 (top right) and L-Ada-2/L-Ste membranes with $\rho_{\text{L-Ada}} = 0$ (bottom left) and 0.2 (bottom right).

There are different reasons accounting for the lipid packing defects. On small length scales, the lipid orientation may be disrupted by the thermal fluctuations, including the transformation to the configuration where lipids are frustrated or out of equilibrium in a transient manner, as seen in our system for the backfolding of L-Ada and also L-Ole or L-Ste. On the top of that, the underlying membrane comprises symmetric- and asymmetric-tailed lipids with distinct molecular shape, which may correspond to different packing properties and membrane orders. The disruption to the packing structure could be triggered, as a consequence of the competition of the membrane order and packing between the two types of lipids, which renders the backfolding of lipids in the form of a collective dynamics as a steady state response.

Note that the presence of L-Ada may effectively destabilize the membrane, which can impair effective encapsulation of RNA that requires LNPs to form stable, curved structures. Thus, it is important to mention an important and favorable property of the L-Ada-containing membrane, which suggests that the backfolding probability does not increase monotonically with the L-Ada fraction. Our simulations show that significant backfolding occurs primarily at low L-Ada concentrations, typically between 10% and 20%. In this range, the membrane remains largely composed of regular L-Ste lipids, preserving both the lamellar structure and bending rigidity. As a result, it is feasible to formulate LNPs that exhibit pronounced lipid backfolding favorable for fusion without compromising membrane rigidity, which is essential for RNA encapsulation and nanoparticle stability.

To attain a better understanding of the driven force and the mechanism of lipid backfolding, we now introduce a simple binary-state model of the L-Ada molecule, either in state A, with its adamantyl tail pointing to the membrane core, or in state B, by exposing the adamantane to an aqueous environment yielding the backfolding state (cf. Figure 6a,b). In state A, the mixture of the adamantyl tail into the lipid acyl chains creates a notable hydrophobic mismatch, leaving a membrane hydrophobic defect in the form of a water-filled hydrophobic cylinder. Assuming the packed acyl chains as a continuum oil medium, the system free energy change after introducing the defect reads[39]

$$\Delta F_A = \gamma_{OW} S_A + \tau (L - L_0)^2 \tag{1}$$

Here, the first term in the right side of eq 1 proportional to the defect surface area S_A refers to the defect energy, with γ_{OW} the surface tension at the oil/water surface. In this study, the adamantane is considered as a rigid sphere with radius R_A, and the circular base of the cylinder defect is deemed equivalent to the cross section $S_s = \pi R_A^2$ of the cylinder, which leads to $S_A = 2S_s + 2\frac{S_s}{R_A}(L - 2R_A)$. The membrane may respond to the defect formation by thinning its oil layer in order to reduce the defect size, which indeed corresponds to the compression of acyl chains in the layer. The energy cost to compress those acyl chains is represented by the lipid chain's conformational free energy in the second term at the right side of eq 1, with τ an entropic spring constant and L_0 the equilibrated lipid length without the defect.

Concerning the state B, the water pore at the oil layer for state A diminishes and exposing the adamantane in aqueous environment gives rise to the energy cost

$$\Delta F_B = \gamma_{OW} S_B \tag{2}$$

where $S_B = 4S_s$ depicts the interfacial area between the adamantane and water. The equation $\Delta F_B = \Delta F_A$ yields the condition with the equal occurrence probability for state A and B. Assuming $\tau \gg 1$ and thus $L \equiv L_c$ in the absence of the structural change of the lipid, we can obtain a marginal ratio

$$\rho_L^* = 3 \tag{3}$$

where $\rho_L = L_0/R_A$ defines the length ratio between the acyl chain and adamantane. $\rho_L > \rho_L^*$ indicates the energetically favorable state of aggregating acyl chains, which may induce the backfolding of adamantanes. ρ_L^* is derived from the perspective of defect size, and the chemistry of the acyl chain and the adamantane that may also influence the backfolding are ignored. Despite that, the above phenomenal model already gives valuable instruction to the lipid design. In our system, we measured $\rho_L = 3.22$ and $\rho_L = 3.43$ by comparing the adamantane size with the acyl chain in the L-Ole and L-Ste molecules, respectively. The model suggests a stronger sign of backfolding of the adamantyl tail in the membrane mixed with the L-Ste molecule, which is in full agreement with the simulation.

According to the model, lipids with a smaller ρ_L exhibit a reduced propensity for backfolding, while those with a larger ρ_L show an enhanced tendency for spontaneous backfolding. In a simplified version of the model, by neglecting structural flexibility, we derived a critical threshold of $\rho_L^* = 3$, above which backfolding becomes energetically favorable. Therefore, this model provides a useful structure-based framework for guiding lipid selection to enhance membrane fusion. This theoretical prediction has been validated by comparing the behavior of the L-Ada/L-Ste system with that of the L-Ada-2/L-Ste system.

Note that the underlying model initially considers only a single L-Ada molecule within the membrane. This simplified picture is most valid in the dilute limit, where the L-Ada lipids are sparsely distributed. As shown in Figure S20, we modeled the interaction between two neighboring L-Ada lipids and the resulting clustering of adamantyl groups. Compared with the isolated case illustrated in Figure 6a, the key difference lies in the enlarged defect area within the lipid core. Accordingly, the defect area S_A in eq 1 must be reformulated to reflect this cooperative effect. Furthermore, this approach can be generalized to describe S_A as a function of n, the number of adjacent adamantyl tails (cf. Figure S21). With that, we can prove that the defect energy ΔF_A quickly saturates with n (see details in the Supporting Information). As a result, the energetic gain from adamantane backfolding diminishes at higher n, thereby suppressing the probability of backfolding in more concentrated L-Ada systems. This prediction is consistent with our simulation results, which show pronounced backfolding behavior at low L-Ada concentrations but a marked reduction in backfolding when L-Ada is present at higher concentrations, where adamantane clustering becomes more prominent.

Lastly, we discuss the role of chain flexibility in the lipid backfolding. This effect has been represented by the harmonic potential in eq 1. According to eq 1, we can first calculate the equilibrated chain length $L = L_0 - \Delta L$ by minimizing F_A with respect to L, yielding $\Delta L = \frac{S_S}{R}\frac{\gamma_{OW}}{\tau}$. Substituting ΔL in eq 1, we can obtain the marginal length ratio

$$\rho_L^* = 3 + \frac{\pi\gamma_{OW}}{2\tau} \tag{4}$$

In the limit of $\tau \gg 1$, $\rho_L^* = 3$ approaches the solution of eq 1 corresponding to a set of rigid lipids. Interestingly, eq 4 suggests $\rho_L^* > 3$ in all cases. Namely, a higher degree of asymmetricity of the lipid tails is generally required to ensure the lipid backfolding when approaching the real lipid molecule with a certain flexibility. Note that the flexible chain grants the biolayer the capacity to suppress the energy defect, only at the expense of a small energy cost to deform the chain. As such, state A having the adamantane inside the membrane becomes in favor, as compared to state B with lipid backfolding.

The above discussion highlights the correlation between the lipid backfolding tendency and tail asymmetry. Building on this, we synthesized a new lipid derivative, L-Ada-2, which is based on L-Ada but with the adamantane tail extended by the addition of two methylene groups (cf. Figure 6c). This modification allows us to estimate the length ratio, denoted as $\rho_L^* = 3.43$ and 2.52, for L-Ada and L-Ada-2, respectively, with ρ_L^* being smaller for L-Ada-2 due to the elongation of the shorter adamantyl tail. According to our model, lipid backfolding is expected to be suppressed as the asymmetry between the lipid tails decreases. In the experiment, for LNPs containing L-Ada and L-Ste, with $\rho_{\text{L-Ada}}$ set from 0 to 0.2, the TE is measured, increasing from 17.67% to 63.40%, while a weaker enhancement in membrane fusion efficiency and TE (21.50−42.73%) is observed compared to LNPs containing L-Ada-2 (cf. Figures 6d,e and S22). The raw data of TE and mean fluorescence intensity of HeLa cells are supplied in Figure S23. This observation aligns exactly with our model's prediction, although it should be noted that the model is purely phenomenological and lacks chemical details.

Note that, line tension is also a crucial factor in the membrane fusion process, as it reflects lipid packing stress, curvature frustration, and interfacial mismatch.[40] One well-known role of line tension is in the hemifusion stalk formation, where it acts as a resistance to the expansion of the stalk, a necessary step for membrane fusion.[41,42] Our study differs from previous work in that we focus not on the lamellar-to-nonlamellar transition but on membranes that already contain a few extruded lipids with hydrophobic tails ready to insert into the incoming membrane. Thus, the issue of line tension is not explicitly discussed here.

To sum up, the above model provides a quantitative description of the aggregation-induced-backfolding behavior for lipids with adamantanes and provides specific principles for designing those lipids with asymmetric tails. The aggregation-induced backfolding behavior permits the engineered emergence of hydrophobic defects on the LNP, and their mechanical properties can be retained after careful tuning of the LNP formulation. These results establish the potential for boosting the RNA TE, from a fundamental level of the lipid design and mixture.

METHODS

Molecular Dynamics Simulations. The initial structure of the binary membrane was generated using genmixmem,[43] with a completely random arrangement of lipid molecules. Each layer consisteds of 100 lipid molecules, a total of 200 molecules. The lipids were initially distributed in a 10 × 10 matrix with a sufficiently small intermolecular distance, ensuring no overlap (cf. Figures S24 and S25). The reference carbon atoms of all lipids in the same leaflet were aligned at the same z position, and the molecules were allowed to rotate randomly. The lipids in the two leaflets were arranged in a nonidentical pattern. The configuration of the initial membrane was optimized through several stages of MD simulations (see details in the Supporting Information). The Amber14sb force field was adopted for running the simulation.[44] To improve the force field accuracy in MD simulations, we employed optimally weighted restrained electrostatic potential (RESP) charges. Specifically, the refined RESP2 method[45] is used, where conformation optimization for the target lipid in water is performed, followed by Multiwfn[46,47] calculations to determine the RESP2 charge in both gas and solution phases. The average of the two values is taken as the atomic charge for the lipids in the simulation. All simulation files are generated using Sobtop.[48]

Measured Quantities. *Lipid Order Parameter.* We separately calculated the order parameter for the lipid, concerning the long hydrocarbon tail (S_{CH}) and that for the adamantyl tail (S_{CC}). The order parameter is calculated by

$$S_{CH} = -1/2\langle 3\cos^2\theta - 1\rangle \tag{5}$$

Here, θ refers to the angle between the z axis and C−H vector for carbon atoms in long tail chains (cf. Figure S26a). For the tail with adamantane, θ describes the similar angle but with respect to the C−C bond connecting the adamantane structure (cf. Figure S26b). $\langle\cdots\rangle$ stands for the ensemble average for all simulated frames lasting at least 50 ns.

The Number of Penetrated Water Molecules. To quantify the extent of water exposure to the membrane hydrophobic core, we defined N_W as the water atoms within 3 Å from all of the atoms of lipid tails. This cutoff distance of 3 Å is equal to the size of a water molecule.

The Membrane Thickness. Luzzati thickness approximates the system comprising two regions. The first region concerns the membrane consisting of all lipids with volume of V_L and the other corresponds to the aqueous solution bearing all water with the volume V_W. The Luzzati thickness D_B reads all water molecules with a volume of V_W, which is equal to the product of water molecules count N_{AW} and the volume of single water molecule V_{SW}.

$$D_B = (V_{box} - N_{AW} \times V_{SW})/A \tag{6}$$

Here, V_{box} and A refer to the volume and the area in the x−y plane of the simulation box, respectively. N_{AW} and V_{SW} measure the water number and the estimated volume for the single water.

The Membrane Bending Rigidity K_C. To assess the membrane rigidity, we calculated the bending rigidity for the membrane according to the real-space fluctuations methodology.[49] The simulation system is first expanded along the x−y direction, to incorporate the periodic boundary condition. We then analyzed the relative orientation of adjacent lipids, as an indicator to the membrane local curvature. The lipid is positionally featured by the mass center of the polar head and the hydrocarbon chains (see the Supporting Information for details). $\boldsymbol{n}$ defines the unit vector pointing from the tail to the lipid head. The reference atom C_g refers to the carbon atom connecting the polar headgroup and hydrocarbon chains. Based on C_g, we may identify the lipid pair defining two lipid molecules within 1 nm (measured by distance vector $\boldsymbol{h}$). For each lipid in the same pair, the covariant derivative S_i for each lipid pair reads

$$S_i = (\boldsymbol{n_i}\cdot\boldsymbol{e} - \boldsymbol{n_j}\cdot\boldsymbol{e})/|\boldsymbol{h}| \tag{7}$$

Here, $\boldsymbol{e}$ is the unit vector parallel to $\boldsymbol{h}$. We calculated $P(S_i)$ as the distribution function of S_i, for each pair type and fit it by Gaussian distribution. After the construction of $P(S_i)$ distribution, fitting of a quadratic function is carried out on it as shown in eq 8. The splay moduli K_C for each pair type are obtained as the coefficient of the quadratic term.

$$-2\frac{k_BT}{A_l}\ln(P(S_i)) = K_C(S_i)^2 + C' \tag{8}$$

Here, A_l is the area per lipid, which can be conveniently measured in the simulation. Bending rigidity K_C for the entire membrane system then follows as the number-averaged from K_C of all pair types.

The Lipid Backfolding Probability P_b and Time T_b. The backfolding lipid is defined as one where the tail extremity moves farther from the membrane core than the reference carbon atom C_g (cf. Figure 2). The tail extremity is identified as the last carbon atom furthest from the headgroup in the tail chains of L-Ole, L-Ste, and the sn2 chains of L-Ada. For the sn1 chains in L-Ada, the center of the terminal six-membered ring in the adamantane structure is considered as the tail extremity. In each simulated frame, all backfolding lipids are identified, allowing for the calculation of backfolding probability $P_{b,i}$ for lipids of type i across all simulated frames. For backfolding time, we measured the longest continuous period during which a lipid molecule remains in the backfolded state in the simulation. Averaging across all lipids of type i gives an estimate of the backfolding duration time $T_{b,i}$, as the largest time for those lipids that maintain backfolding behavior throughout the simulation.

Calculation of Cluster Size S_b. Adjacent backfolding lipids form a distinct patch on the membrane, highlighting areas with pronounced packing defects. To identify these patches, we defined adjacent lipids as those where any atom in one lipid molecule is within 3 Å of an atom in another lipid (cf. Figure S27). Using this criterion, we can identify all back-folding patches on the membrane. The size of the largest patch for all lipids in the simulation is reported as S_b, measuring the extent of the most prominent backfolding patch revealed during the simulation.

Synthesis of Various Lipids, Lipid Nanoparticles Preparation, and Measurements of Membrane Fusion Efficiency. Experimental details can be found in the Supporting Information.

ASSOCIATED CONTENT

Supporting Information

The Supporting Information is available free of charge at https://pubs.acs.org/doi/10.1021/acsnano.5c07140.

> Detailed methods for MD simulations; definitions and calculations of physical properties; physical model for initial stage of membrane fusion; synthesis of lipids; preparation of LNPs; measurements of TE; and raw TE percentage (PDF)

AUTHOR INFORMATION

Corresponding Authors

Xiao Xu − *School of Chemistry and Chemical Engineering, Nanjing University of Science and Technology, Nanjing 210094, P. R. China;* orcid.org/0000-0001-9820-3153; Email: xuxiao@njust.edu.cn

Can Zhang − *State Key Laboratory of Natural Medicines, China Pharmaceutical University, Nanjing 211198, P. R. China;* orcid.org/0000-0003-3529-5438; Email: zhangcan@cpu.edu.cn

Authors

Guan Wang − *State Key Laboratory of Natural Medicines, China Pharmaceutical University, Nanjing 211198, P. R. China*

Mengtong Wu − *State Key Laboratory of Natural Medicines, China Pharmaceutical University, Nanjing 211198, P. R. China*

Juanjuan Ye − *State Key Laboratory of Natural Medicines, China Pharmaceutical University, Nanjing 211198, P. R. China*

Yazhou Xu − *State Key Laboratory of Natural Medicines, China Pharmaceutical University, Nanjing 211198, P. R. China*

Yuxiao Chen − *State Key Laboratory of Natural Medicines, China Pharmaceutical University, Nanjing 211198, P. R. China*

Caoyun Ju − *State Key Laboratory of Natural Medicines, China Pharmaceutical University, Nanjing 211198, P. R. China*

Complete contact information is available at: https://pubs.acs.org/10.1021/acsnano.5c07140

Author Contributions

G.W. designed the studies and performed all MD simulations. Data analysis is carried out by G.W. and Y.C. M.W. carried out all the synthesis work. Membrane fusion experiments were carried out by M.W., J.Y. and Y.X. G.W. and X.X. wrote the manuscript. C.J., X.X., and C.Z. supervised the work.

Notes

The authors declare no competing financial interest.

ACKNOWLEDGMENTS

The authors acknowledge the National Science Foundation of China (21903045) for financial support.

REFERENCES

(1) Naldini, L. Gene therapy returns to centre stage. *Nature* **2015**, *526*, 351−360.

(2) Zhang, Y.; Sun, C.; Wang, C.; Jankovic, K. E.; Dong, Y. Lipids and lipid derivatives for RNA delivery. *Chem. Rev.* **2021**, *121*, 12181−12277.

(3) Dammes, N.; Peer, D. Paving the road for RNA therapeutics. *Trends Pharmacol. Sci.* **2020**, *41*, 755−775.

(4) Foldvari, M.; Chen, D. W.; Nafissi, N.; Calderon, D.; Narsineni, L.; Rafiee, A. Non-viral gene therapy: Gains and challenges of non-invasive administration methods. *J. Controlled Release* **2016**, *240*, 165−190.

(5) Paunovska, K.; Loughrey, D.; Dahlman, J. E. Drug delivery systems for RNA therapeutics. *Nat. Rev. Genet.* **2022**, *23*, 265−280.

(6) Chatterjee, S.; Kon, E.; Sharma, P.; Peer, D. Endosomal escape: A bottleneck for LNP-mediated therapeutics. *Proc. Natl. Acad. Sci. U.S.A.* **2024**, *121*, No. e2307800120.

(7) Ozpolat, B.; Sood, A. K.; Lopez-Berestein, G. Liposomal siRNA nanocarriers for cancer therapy. *Adv. Drug Delivery Rev.* **2014**, *66*, 110−116.

(8) Allen, T. M.; Cullis, P. R. Liposomal drug delivery systems: from concept to clinical applications. *Adv. Drug Delivery Rev.* **2013**, *65*, 36−48.

(9) Wan, C.; Allen, T.; Cullis, P. Lipid nanoparticle delivery systems for siRNA-based therapeutics. *Drug Delivery Transl. Res.* **2014**, *4*, 74−83.

(10) Hou, X.; Zaks, T.; Langer, R.; Dong, Y. Lipid nanoparticles for mRNA delivery. *Nat. Rev. Mater.* **2021**, *6*, 1078−1094.

(11) Tenchov, R.; Bird, R.; Curtze, A. E.; Zhou, Q. Lipid nanoparticles-from liposomes to mRNA vaccine delivery, a landscape of research diversity and advancement. *ACS Nano* **2021**, *15*, 16982−17015.

(12) Dolgin, E. Better lipids to power next generation of mRNA vaccines. *Science* **2022**, *376*, 680−681.

(13) Gindy, M. E.; DiFelice, K.; Kumar, V.; Prud'homme, R. K.; Celano, R.; Haas, R. M.; Smith, J. S.; Boardman, D. Mechanism of macromolecular structure evolution in self-assembled lipid nanoparticles for siRNA delivery. *Langmuir* **2014**, *30*, 4613−4622.

(14) Leung, A. K.; Tam, Y. Y. C.; Chen, S.; Hafez, I. M.; Cullis, P. R. Microfluidic mixing: a general method for encapsulating macromolecules in lipid nanoparticle systems. *J. Phys. Chem. B* **2015**, *119*, 8698−8706.

(15) Zu, H.; Gao, D. Non-viral vectors in gene therapy: recent development, challenges, and prospects. *AAPS J.* **2021**, *23*, 78.

(16) Gilleron, J.; Querbes, W.; Zeigerer, A.; Borodovsky, A.; Marsico, G.; Schubert, U.; Manygoats, K.; Seifert, S.; Andree, C.; Stöter, M.; et al. Image-based analysis of lipid nanoparticle−mediated siRNA delivery, intracellular trafficking and endosomal escape. *Nat. Biotechnol.* **2013**, *31*, 638−646.

(17) Wittrup, A.; Ai, A.; Liu, X.; Hamar, P.; Trifonova, R.; Charisse, K.; Manoharan, M.; Kirchhausen, T.; Lieberman, J. Visualizing lipid-formulated siRNA release from endosomes and target gene knockdown. *Nat. Biotechnol.* **2015**, *33*, 870−876.

(18) Behr, J.-P. The proton sponge: a trick to enter cells the viruses did not exploit. *Chimia* **1997**, *51*, 34.

(19) Xu, Z. P. G. Strategy for cytoplasmic delivery using inorganic particles. *Pharm. Res.* **2022**, *39*, 1035−1045.

(20) Won, Y.-Y.; Sharma, R.; Konieczny, S. F. Missing pieces in understanding the intracellular trafficking of polycation/DNA complexes. *J. Controlled Release* **2009**, *139*, 88.

(21) Kanasty, R.; Dorkin, J. R.; Vegas, A.; Anderson, D. Delivery materials for siRNA therapeutics. *Nat. Mater.* **2013**, *12*, 967−977.

(22) Eygeris, Y.; Gupta, M.; Kim, J.; Sahay, G. Chemistry of lipid nanoparticles for RNA delivery. *Acc. Chem. Res.* **2022**, *55*, 2−12.

(23) Smith, S. A.; Selby, L. I.; Johnston, A. P.; Such, G. K. The endosomal escape of nanoparticles: toward more efficient cellular delivery. *Bioconjugate Chem.* **2019**, *30*, 263−272.

(24) Zuhorn, I. S.; Bakowsky, U.; Polushkin, E.; Visser, W. H.; Stuart, M. C.; Engberts, J. B.; Hoekstra, D. Nonbilayer phase of lipoplex−membrane mixture determines endosomal escape of genetic cargo and transfection efficiency. *Mol. Ther.* **2005**, *11*, 801−810.

(25) Koltover, I.; Salditt, T.; Rädler, J. O.; Safinya, C. R. An inverted hexagonal phase of cationic liposome-DNA complexes related to DNA release and delivery. *Science* **1998**, *281*, 78−81.

(26) Yu, H.; Iscaro, J.; Dyett, B.; Zhang, Y.; Seibt, S.; Martinez, N.; White, J.; Drummond, C. J.; Bozinovski, S.; Zhai, J. Inverse cubic and hexagonal mesophase evolution within ionizable lipid nanoparticles correlates with mRNA transfection in macrophages. *J. Am. Chem. Soc.* **2023**, *145*, 24765−24774.

(27) Yu, H.; Angelova, A.; Angelov, B.; Dyett, B.; Matthews, L.; Zhang, Y.; El Mohamad, M.; Cai, X.; Valimehr, S.; Drummond, C. J.; et al. Real-Time pH-Dependent Self-Assembly of Ionisable Lipids from COVID-19 Vaccines and In Situ Nucleic Acid Complexation. *Angew. Chem., Int. Ed.* **2023**, *62*, No. e202304977.

(28) Philipp, J.; Dabkowska, A.; Reiser, A.; Frank, K.; Krzysztoń, R.; Brummer, C.; Nickel, B.; Blanchet, C. E.; Sudarsan, A.; Ibrahim, M.; et al. pH-dependent structural transitions in cationic ionizable lipid mesophases are critical for lipid nanoparticle function. *Proc. Natl. Acad. Sci. U.S.A.* **2023**, *120*, No. e2310491120.

(29) Jayaraman, M.; Ansell, S. M.; Mui, B. L.; Tam, Y. K.; Chen, J.; Du, X.; Butler, D.; Eltepu, L.; Matsuda, S.; Narayanannair, J. K.; et al. Maximizing the potency of siRNA lipid nanoparticles for hepatic gene silencing in vivo. *Angew. Chem., Int. Ed.* **2012**, *124*, 8657−8661.

(30) Semple, S. C.; Akinc, A.; Chen, J.; Sandhu, A. P.; Mui, B. L.; Cho, C. K.; Sah, D. W.; Stebbing, D.; Crosley, E. J.; Yaworski, E.; et al. Rational design of cationic lipids for siRNA delivery. *Nat. Biotechnol.* **2010**, *28*, 172−176.

(31) Pattipeiluhu, R.; Zeng, Y.; Hendrix, M. M. R. M.; Voets, I. K.; Kros, A.; Sharp, T. H. Liquid crystalline inverted lipid phases encapsulating siRNA enhance lipid nanoparticle mediated transfection. *Nat. Commun.* **2024**, *15*, 1303.

(32) Zhigaltsev, I. V.; Maurer, N.; Wong, K. F.; Cullis, P. R. Triggered release of doxorubicin following mixing of cationic and anionic liposomes. *Biochim. Biophys. Acta, Biomembr.* **2002**, *1565*, 129−135.

(33) Lokugamage, M. P.; Sago, C. D.; Gan, Z.; Krupczak, B. R.; Dahlman, J. E. Constrained nanoparticles deliver siRNA and sgRNA to T cells in vivo without targeting ligands. *Adv. Mater.* **2019**, *31*, 1902251.

(34) Zhang, C.; Cao, Y.; Li, J.; Wu, M.; Xue, L. A pharmaceutical composition and its use. CN 118222627 A, 2024.

(35) Martens, S.; McMahon, H. T. Mechanisms of membrane fusion: disparate players and common principles. *Nat. Rev. Mol. Cell Biol.* **2008**, *9*, 543−556.

(36) Bentz, J. Membrane fusion mediated by coiled coils: a hypothesis. *Biophys. J.* **2000**, *78*, 886−900.

(37) Smirnova, Y. G.; Marrink, S.-J.; Lipowsky, R.; Knecht, V. Solvent-exposed tails as prestalk transition states for membrane fusion at low hydration. *J. Am. Chem. Soc.* **2010**, *132*, 6710−6718.

(38) Vanni, S.; Vamparys, L.; Gautier, R.; Drin, G.; Etchebest, C.; Fuchs, P. F.; Antonny, B. Amphipathic lipid packing sensor motifs: probing bilayer defects with hydrophobic residues. *Biophys. J.* **2013**, *104*, 575−584.

(39) Watson, M. C.; Penev, E. S.; Welch, P. M.; Brown, F. L. H. Thermal fluctuations in shape, thickness, and molecular orientation in lipid bilayers. *J. Chem. Phys.* **2011**, *135*, 244701.

(40) Chernomordik, L. V.; Kozlov, M. M. Mechanics of membrane fusion. *Nat. Struct. Mol. Biol.* **2008**, *15*, 675−683.

https://doi.org/10.1021/acsnano.5c07140

(41) Risselada, H. J.; Bubnis, G.; Grubmüller, H. Expansion of the fusion stalk and its implication for biological membrane fusion. *Proc. Natl. Acad. Sci. U.S.A.* **2014**, *111*, 11043−11048.

(42) Gao, L.; Lipowsky, R.; Shillcock, J. Tension-induced vesicle fusion: pathways and pore dynamics. *Soft Matter* **2008**, *4*, 1208−1214.

(43) Lu, T. *genmixmem Is a Tool for Generating Structure Files of Phospholipid Bilayer Membranes of Mixed Components*. http://sobereva.com/245 (accessed 17 August 2023).

(44) Maier, J. A.; Martinez, C.; Kasavajhala, K.; Wickstrom, L.; Hauser, K. E.; Simmerling, C. ff14SB: improving the accuracy of protein side chain and backbone parameters from ff99SB. *J. Chem. Theory Comput.* **2015**, *11*, 3696−3713.

(45) Schauperl, M.; Nerenberg, P. S.; Jang, H.; Wang, L.-P.; Bayly, C. I.; Mobley, D. L.; Gilson, M. K. Non-bonded force field model with advanced restrained electrostatic potential charges (RESP2). *Commun. Chem.* **2020**, *3*, 44.

(46) Lu, T.; Chen, F. Multiwfn: A multifunctional wavefunction analyzer. *J. Comput. Chem.* **2012**, *33*, 580−592.

(47) Lu, T. A comprehensive electron wavefunction analysis toolbox for chemists, Multiwfn. *J. Chem. Phys.* **2024**, *161*, 082503.

(48) Lu, T. *Sobtop: A Tool of Generating Forcefield Parameters and GROMACS Topology File, Version 1.0(dev3.1)*. http://sobereva.com/soft/Sobtop (accessed 1 April 2023).

(49) Doktorova, M.; Harries, D.; Khelashvili, G. Determination of bending rigidity and tilt modulus of lipid membranes from real-space fluctuation analysis of molecular dynamics simulations. *Phys. Chem. Chem. Phys.* **2017**, *19*, 16806−16818.